Supplemental Information

High-dimensional time-frequency entanglement in a singly-filtered biphoton frequency comb

Xiang Cheng[1†*], Kai-Chi Chang[1†*], Murat Can Sarihan[1], Andrew Mueller[2,3], Maria Spiropulu[4], Matthew D. Shaw[2], Boris Korzh[2], Andrei Faraon[5], Franco N. C. Wong[6], Jeffrey H. Shapiro[6], and Chee Wei Wong[1*]

[1] Fang Lu Mesoscopic Optics and Quantum Electronics Laboratory, Department of Electrical and Computer Engineering, University of California, Los Angeles, CA 90095, USA

[2] Jet Propulsion Laboratory, California Institute of Technology, 4800 Oak Grove Dr., Pasadena, CA 91109, USA

[3] Applied Physics, California Institute of Technology, 1200 E California Blvd, Pasadena, CA 91125, USA

[4] Division of Physics, Mathematics and Astronomy, California Institute of Technology, Pasadena, CA 91125, USA

[5] Thomas J. Watson, Sr., Laboratory of Applied Physics, California Institute of Technology, Pasadena, CA 91125, USA

[6] Research Laboratory of Electronics, Massachusetts Institute of Technology, Cambridge, MA 02139, USA

† These authors contributed equally

* email: chengxiang@ucla.edu; uclakcchang@ucla.edu; cheewei.wong@ucla.edu

This Supplementary Information contains the following notes:

Supplementary Note 1. Theory for the singly-filtered biphoton frequency comb's signal-idler cross- correlation function

In this section we derive and evaluate the signal-idler cross-correlation function for the singly-filtered biphoton frequency comb (BFC) under the assumption of near-pure-state SPDC biphoton generation. Before doing so, however, we will replace the *approximate* result for that BFC's frequency-domain (unnormalized) biphoton wave function,

$$\psi(\Omega) = \sum_{m=-N}^{N} \frac{\mathrm{sinc}(A\Omega)}{\Delta\omega + i(\Omega - m\Delta\Omega)}, \tag{1}$$

from the main text's Eq. (1), with the *exact* result [S1],

$$\psi(\Omega) = \frac{\mathrm{sinc}(\Omega t_{\mathrm{coh}}/2) e^{-4\Omega^2 \ln(2)/\Delta\omega_c^2} e^{-i\Omega t_{\mathrm{coh}}/2}}{1 + i\frac{\Delta\Omega}{\pi\Delta\omega}\sin(\pi\Omega/\Delta\Omega) e^{-i\pi\Omega/\Delta\Omega}}, \tag{2}$$

where $t_{\mathrm{coh}} = 2A = 2.78/\pi B_{\mathrm{PM}} = 3.61$ ps is the coherence time associated with the $B_{\mathrm{PM}} = 245$ GHz full-width half-maximum (FWHM) phase-matching bandwidth, $\Delta\Omega = 45.32$ GHz is the fiber Fabry-Pérot cavity's (FFPC's) free spectral range (FSR), $\Delta\omega/\pi = 1.56$ GHz is the FFPC's FWHM linewidth, and $\Delta\omega_c/\pi = 225$ GHz is the FWHM bandwidth of the 1.3 nm bandpass filter (BPF) used to clean the signal and idler spectra produced by spontaneous parametric down-conversion (SPDC) in our periodically-poled $KTiOPO_4$ (ppKTP) waveguide.

The exact result from Eq. (2) differs in three ways from the main text's approximate form shown above in Eq. (1):

1. Equation (1) assumes a brickwall bandpass filter,

$$H_{\mathrm{BPF}}(\Omega) = \begin{cases} 1, |\Omega| \le \Delta\omega_c, \\ 0, \text{otherwise}, \end{cases}$$

whereas the actual bandpass filter used had the Gaussian frequency response,

$$H_{\mathrm{BPF}}(\Omega) = e^{-\frac{4\Omega^2 \ln(2)}{\Delta\omega_c^2}},$$

of the same FWHM bandwidth.

2. Equation (1) treats the FFPC's filtering action as the sum of Lorentzian lineshapes, each with FWHM bandwidth $2\Delta\omega$, that are centered at integer multiples of the cavity's FSR, whereas Eq. (2) uses the cavity's exact frequency response,

$$H_{\mathrm{FFPC}}(\Omega) = \frac{1}{1 + i\frac{\Delta\Omega}{\pi\Delta\omega}\sin(\pi\Omega/\Delta\Omega)e^{-i\pi\Omega/\Delta\Omega}}.$$

3. Equation (2) includes the phase-delay term, $e^{-i\Omega t_{\mathrm{coh}}//2}$, associated with the SPDC source's idler beam having a higher group velocity, in the ppKTP waveguide, than that source's signal beam.

Armed with the singly-filtered BFC's biphoton exact wave function from Eq. (2), we are now ready to evaluate its coincidence-counting (second-order) signal-idler cross-correlation function. The frequency-domain biphoton wave function produced by continuous-wave (cw) SPDC, after filtering by the BPF and FFPC, is proportional to the phase-sensitive cross-spectrum of the post-filtered signal and idler's photon-units baseband field operators in the exact, Gaussian-state theory of cw SPDC, viz. [S1],

$$\psi(\Omega) \propto S_{SI}^{(p)}(\Omega) \equiv \int d\tau \left\langle \hat{E}_S(t+\tau)\, \hat{E}_I(t) \right\rangle e^{-i\Omega\tau}, \tag{3}$$

where angle brackets denote quantum average. In the absence of detector timing jitter, it then follows – see, e.g., [S2] for an example of Gaussian-state coincidence-counting analysis – that the cross-correlation function we are seeking satisfies

$$R_{SI}(\tau) \propto |\Psi(\tau)|^2, \tag{4}$$

where $\Psi(t)$ is the singly-filtered BFC's (unnormalized) time-domain biphoton wave function, i.e., the inverse Fourier transform of $\psi(\Omega)$. Because our detectors do have timing jitter, the *observed* cross-correlation becomes

$$R_{SI}^{\mathrm{obs}}(\tau) = \int d\mu\, R_{SI}(\mu) \frac{\exp[-(\tau-\mu)^2/2t_j^2]}{\sqrt{2\pi t_j^2}}, \tag{5}$$

where we have assumed a zero-mean, variance t_j^2, Gaussian-distributed combined timing jitter from the two detectors.

From Eqs. (2) and (4) it can be shown that $R_{SI}(\tau)$ has recurring peaks at $\tau = t_{\mathrm{coh}}/2 + n\Delta T$ for $n = 0, 1, 2, \ldots$, where $\Delta T = 2\pi/\Delta\Omega = 22.1$ ps is the cavity round-trip time, but going forward we will suppress their $t_{\mathrm{coh}}/2$ offset from $n\Delta T$. These peaks are increasingly blurred by detector timing jitter as t_j increases, and can easily be washed out. To quantify this behavior, we used the results presented above to numerically evaluate

$$\tilde{R}_{SI}(\tau) \equiv \frac{R_{SI}^{\mathrm{obs}}(\tau - \tau_{\mathrm{max}})}{R_{SI}^{\mathrm{obs}}(\tau_{\mathrm{max}})}, \quad (6),$$

where τ_{max} is the time at which $R_{SI}^{\mathrm{obs}}(\tau)$ takes on its maximum value. This form of the correlation function achieves its peak value, $\max_{\tau} \tilde{R}_{SI}(\tau) = 1$, at $\tau = 0$, regardless of root-mean-square (rms) timing jitter t_j, thus making it well suited to display the impact of timing jitter on the observed signal and idler's coincidence-counting cross-correlation, as seen in the main text's Figure 1b.

In Supplementary Figure 1, we plot three examples of $\tilde{R}_{SI}(\tau)$ versus τ in ns for the source parameters of our 45.32 GHz singly-filtered BFC: $t_j = 0.78$ ps (blue curve), $t_j = 7.8$ ps (red curve), and $t_j = 74$ ps (black curve). In the main text's Figure 1b, we show good agreement between our experiment and the theoretical result when $t_j = 74$ ps. Although the temporal oscillation signature of the singly-filtered BFC is completely blurred out by the timing jitter in our measurements, our modeling clearly shows that as $t_j/\Delta T$ decreases the comb structure can be resolved [S3]. For example, when $t_j = 7.8$ ps, the singly-filtered BFC's structure produced by our 45.32 GHz FSR, 1.56 GHz FWHM bandwidth FFPC can be seen in $\tilde{R}_{SI}(\tau)$. Moreover, with $t_j = 0.78$ ps, near-perfect cavity resonances appear in $\tilde{R}_{SI}(\tau)$, and we note that such low-jitter SNSPDs have been demonstrated recently [S4].

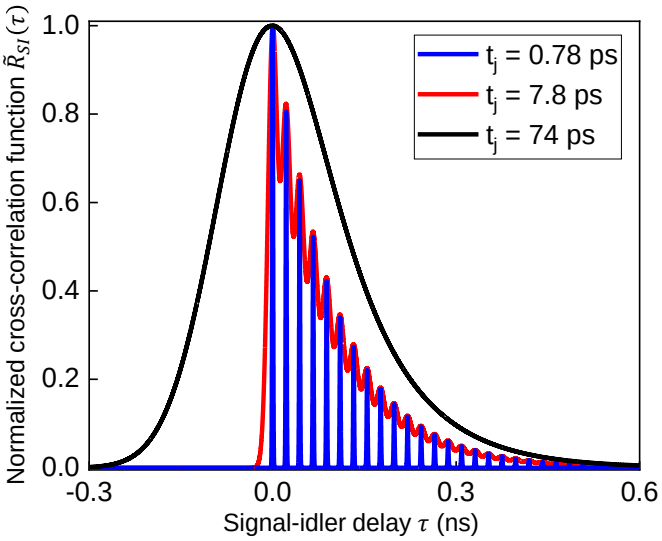

Supplementary Figure 1 | Effect of timing jitter on the normalized coincidence-counting (second-order) signal-idler cross-correlation function $\tilde{R}_{SI}(\tau)$ plotted versus signal-idler delay τ in ns – for the source parameters of our 45.32 GHz singly-filtered BFC. The three cases shown are: $t_j = 0.78$ ps (blue curve), $t_j = 7.8$ ps (red curve), and $t_j = 74$ ps (black curve).

Supplementary Note 2. Heralded single-photon second-order auto-correlation measurements for the singly-filtered biphoton frequency comb

In this section we present additional information about the heralded $g^{(2)}(0)$ auto-correlation measurements of the singly-filtered BFC. The BFC was obtained by passing the signal and idler beams from our SPDC waveguide through the 1.3 nm FWHM bandwidth BPF and then passing the signal beam through the 45.32 GHz FSR, 1.56 GHz FWHM linewidth FFPC. The heralded $g^{(2)}(0)$ was measured as follows: (1) the idler beam was split in two by a 50-50 beam splitter whose outputs were directed to superconducting nanowire single-photon detectors (SNSPDs); (2) SNSPD detection of a signal photon was used as a herald; and (3) a heralded $g^{(2)}(0)$ event was recorded when there was a triple (signal-idler-idler) coincidence with no time offset. At 0.2 mW pump power we measured $g^{(2)}(0) \approx 0.154$. Exchanging the roles of signal and idler, so that the idler illuminated the heralding detector while the signal beam illuminated the 50-50 beam splitter, we obtained $g^{(2)}(0) \approx 0.130$ at 0.6 mW pump power. Both results are well below the classical threshold [S5]. Moreover, because the signal beam's singles rate is considerably lower than the idler's, reliable idler-heralded $g^{(2)}(0)$ measurements could not be obtained at as low a pump power as signal-heralded measurements could. Supplementary Figure 2 shows the expected effect on $g^{(2)}(0)$

of increased pump power, viz., $g^{(2)}(0)$ increases because of increased presence of multi-pair emissions from the SPDC source. We note that the non-zero values of heralded $g^{(2)}(0)$ are primarily due to multi-pair SPDC emissions. Also, the idler-heralded $g^{(2)}(0)$ is lower than the signal-heralded $g^{(2)}(0)$ because it is less likely that two signal photons could survive the higher losses in the signal channel to produce a coincidence.

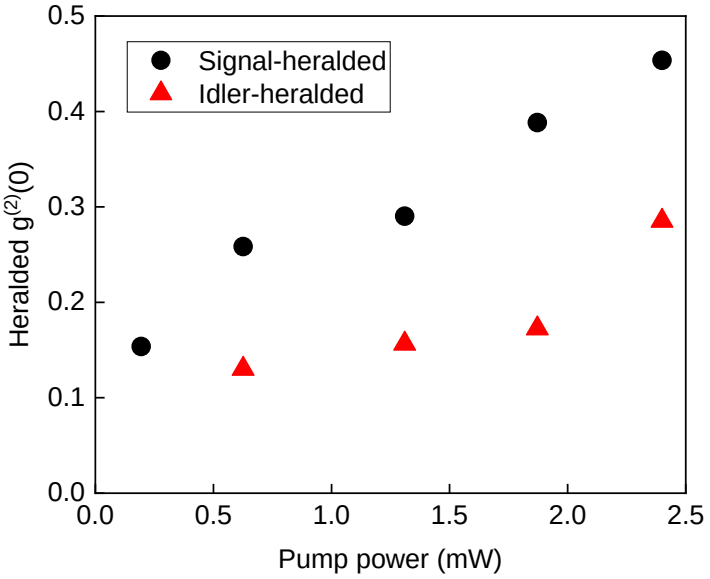

Supplementary Figure 2 | Measured heralded $g^{(2)}(0)$ values versus the pump power for the 45.32 GHz singly-filtered BFC: signal-heralded measurements (black points), idler-heralded measurements (red points).

Supplementary Note 3. Franson-interference recurrences of the singly-filtered biphoton frequency comb

3.A. Theory for the Franson-interference recurrences

In this section we present the theory for the singly-filtered BFC's Franson-interference recurrences. With accidentals subtracted, Ref. [S2]'s results – with its dispersive terms suppressed – lead to the following expression for the normalized (time-average value = 1) envelope of the (accidentals subtracted) Franson-interference recurrences as a function of the idler-signal (arm 1 – arm 2 in the main text's Figure 1a) relative delay, $\delta\tau$:

$$C_{\pm}(\delta\tau) = 1 \pm \frac{2\int_0^{Tg} d\tau\, \mathrm{Re}[K_{SI}^{(p)}(\tau)K_{SI}^{(p)*}(\tau+\delta\tau)]}{\int_0^{Tg} d\tau\left[\left|K_{SI}^{(p)}(\tau)\right|^2+\left|K_{SI}^{(p)}(\tau+\delta\tau)\right|^2\right]}. \quad (7)$$

Here, T_g is the duration of the coincidence gate, and $K_{SI}^{(p)}(\tau)$ is the phase-sensitive cross correlation of the singly-filtered BFC's photon-units, baseband field operators,

$$K_{SI}^{(p)}(\tau) \equiv \left\langle \hat{E}_S(t+\tau)\hat{E}_I(t) \right\rangle = \int \frac{d\Omega}{2\pi} S_{SI}^{(p)}(\Omega) e^{i\Omega\tau}. \quad (8)$$

So, because the singly-filtered BFC's frequency-domain biphoton wave function, $\psi(\Omega)$, is proportional to the phase-sensitive cross spectrum, $S_{SI}^{(p)}(\Omega)$, from Gaussian-state theory, Eq. (7) can be evaluated numerically from using $\psi(\Omega)$ from Eq. (2) in lieu of $S_{SI}^{(p)}(\Omega)$ in Eq. (8) to obtain a result proportional to $K_{SI}^{(p)}(\tau)$. Using that result in numerically evaluating Eq. (7) then yields the desired envelope function for the (accidentals subtracted) Franson-interference recurrences. Using the source parameters for our 45.32 GHz singly-filtered BFC and $T_g = 2$ ns, we obtained the results shown in main text's Figure 2b for -340 ps $\leq \delta\tau \leq$ 340 ps. As shown in main text's Figure 2, our measured (accidentals subtracted) visibility peaks for $0 \leq \delta\tau \leq$ 340 ps are in excellent agreement with our theoretical predictions; with our equipment setup we could not access negative $\delta\tau$ values.

3.B. Pump laser stabilization for the Franson interference measurements

For all the sub-femtosecond-scale Franson interference measurements performed in this work, long-term pump laser stability is a key requirement. Therefore, we custom built a stabilized self-injection locking pump laser with center wavelength around 658 nm. The Littman–Metcalf configuration allows us to stabilize and fine-tune its wavelength for optimizing SPDC photon-pair generation. We measured the laser's wavelength stability with a wavelength meter (Bristol Instruments model 671). The wavelength drift was ≈ 50 MHz over 3.5 hours, as shown in Supplementary Figure 3.

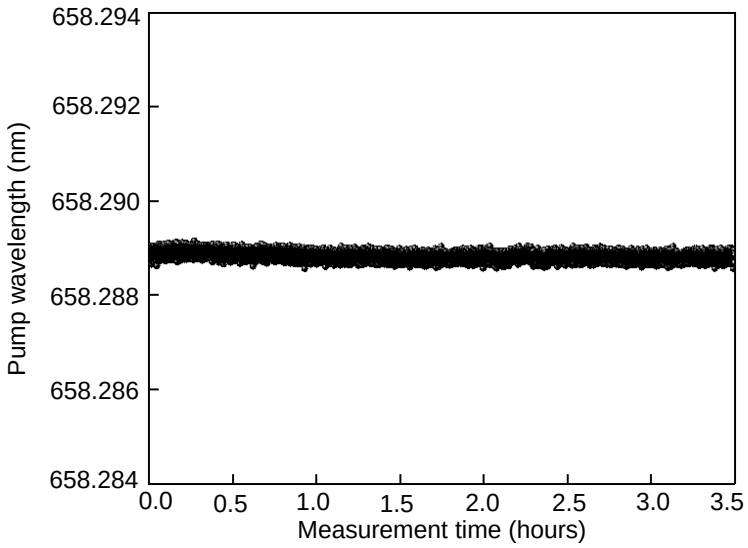

Supplementary Figure 3 | Long-term stability of the 658 nm pump laser with self-injection locking.

3.C. Comparison between Franson-interference recurrences for singly-filtered and doubly-filtered biphoton frequency combs

Here, in Supplementary Figure 4, we compare visibilities of the Franson-interference recurrences for singly-filtered and doubly-filtered 45.32 GHz BFCs, showing theory results for both as well as experimental results for the singly-filtered case. Theory for the singly-filtered BFC was obtained by the procedure described in Supplementary Note 3.A. Theory for the doubly-filtered BFC was obtained by the same procedure using the doubly-filtered version of Eq. (1) for its (unnormalized) frequency-domain biphoton wave function, i.e.,

$$\psi(\Omega) = \sum_{m=-N}^{N} \frac{\mathrm{sinc}(A\Omega)}{|\Delta\omega + i(\Omega - \mathrm{m}\Delta\Omega)|^2}, \tag{9}$$

with the same N, A, Ω, $\Delta\omega$, and $\Delta\Omega$ as the singly-filtered case.

From Supplementary Figure 4, we see that the visibilities for the singly-filtered BFC's recurrences decay more rapidly than those of the doubly-filtered BFC. This behavior is easily understood from Eqs. (1) and (9). Specifically, because the signal and idler are both FFPC filtered in the doubly-filtered case, its frequency-domain biphoton wave function decays more rapidly with increasing frequency than does that of the singly-filtered BFC, for which only the signal beam is FFPC filtered. Consequently, by Fourier duality, the time-domain biphoton wave function of the singly-filtered BFC with increasing time delay decays more rapidly than that of the doubly-filtered

BFC. From Eq. (7), with $K_{SI}^{(p)}(\tau) \propto \Psi(\tau)$, we have our explanation for these sources' behaviors in Supplementary Figure 4.

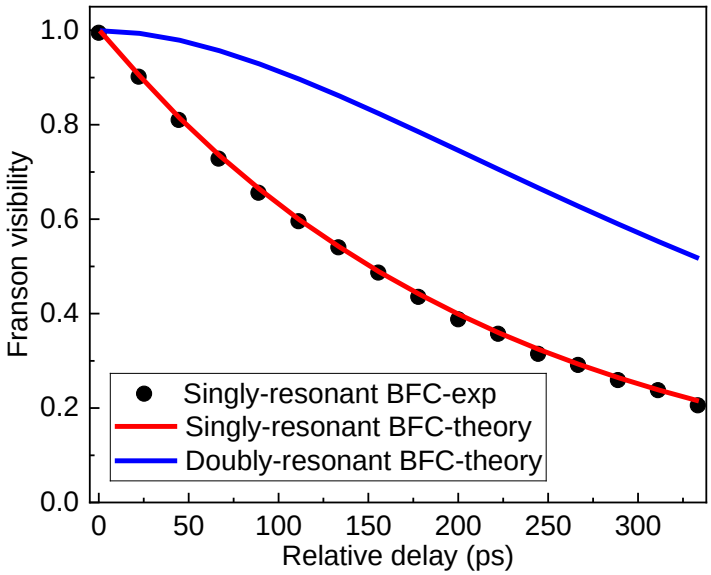

Supplementary Figure 4 | Comparison between theoretical time-bin visibilities of the 45.32 GHz singly-filtered and doubly-filtered BFCs Franson-interference recurrences. Also shown are the experimental results for the singly-filtered case.

3.D. Franson-interference recurrences from singly-filtered biphoton frequency comb after 10 km distribution

Here, in Supplementary Figure 5, we present the measured Franson-interference patterns, after the 10-km asymmetric entanglement distribution described in the main text, for all 16 time bins. The highest measured visibility, 98.81%, was obtained for the 0^{th} time bin. The visibilities for bins 0 through 3 exceeded the 70.7% value needed to violate the Bell's inequality, and those for bins 0 through 6 exceeded the 50% value that is the classical limit. Together, these results clearly show, for the first time, high-quality entanglement distribution of a singly-filtered BFC. Furthermore, comparing Supplementary Figure 5's results to those in the main text's Figure 2c, we find that the average reduction in Franson-interference visibility after 10 km propagation is only 1.21%, showing the high-quality asymmetric entanglement distribution at 10 km distance with our singly-filtered BFC.

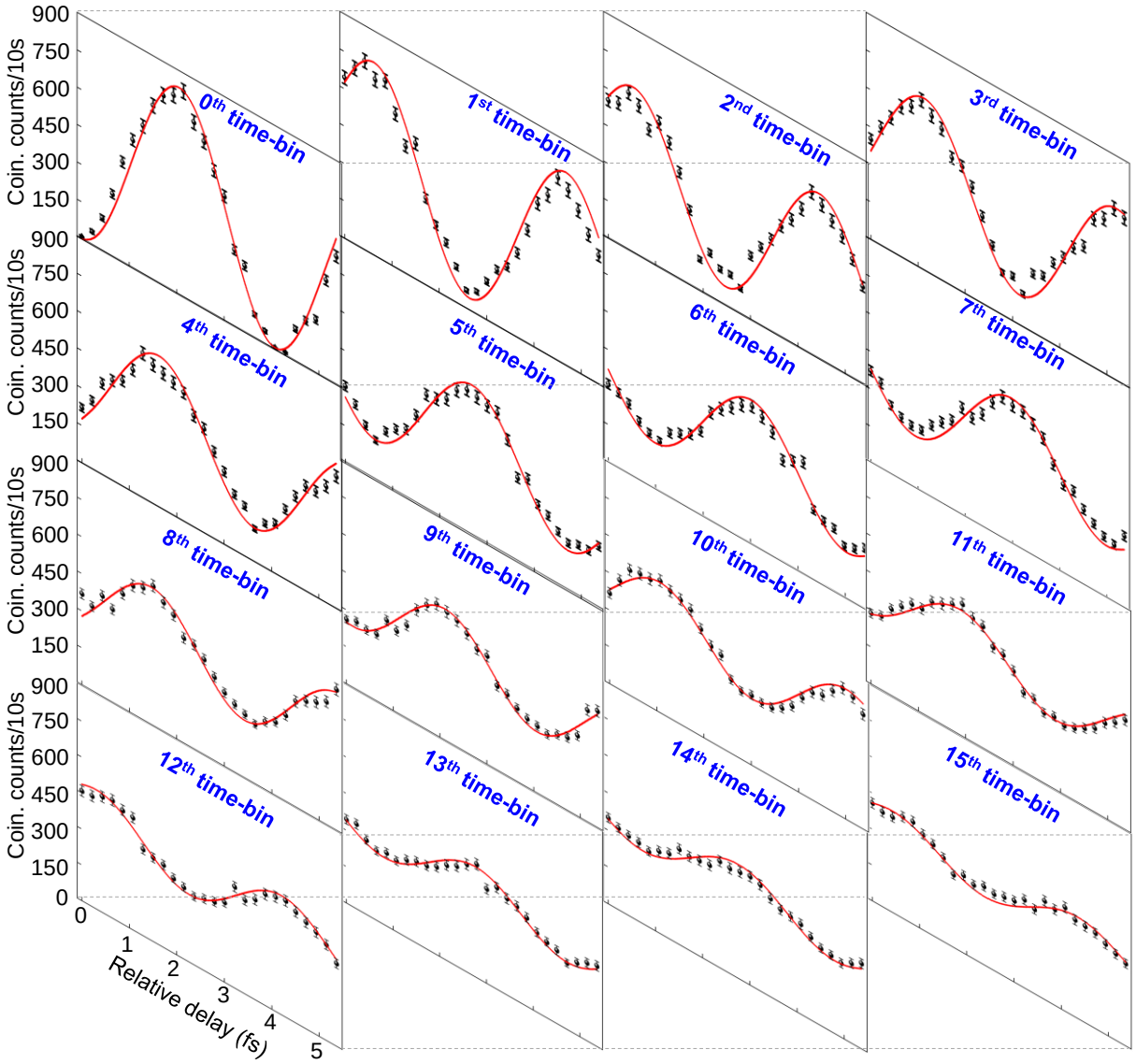

Supplementary Figure 5 | Franson interference fringes – obtained with a 2 ns duration coincidence gate and accidentals subtracted – for 16 time bins of a 45.32 GHz singly-filtered BFC after a 10 km asymmetric entanglement distribution. The highest visibility, 98.81 ± 0.61%, is observed for the central (0^{th}) time bin; bins 0 through 3 have visibilities exceeding the 70.7% value needed to violate Bell's inequality; and bins 0 through 6 have visibilities exceeding the 50% value that is the classical limit. These results clearly demonstrate high-quality 10 km asymmetric distribution of the singly-filtered BFC's time-binned energy-time entanglement. The error bars represent one standard deviation of the mean assuming Poissonian statistics.

We also compared the experimental time-bin visibilities for the post-distribution Franson interference recurrences with Supplementary Note 3.A's theory, which presumes perfect entanglement distribution. Our results are shown both in the main text's Figure 4b and in Supplementary Figure 6. The average deviation of experiment from theory is ≈ 4.25%, indicating efficient distribution of our singly-filtered BFC's time-binned energy-time entanglement.

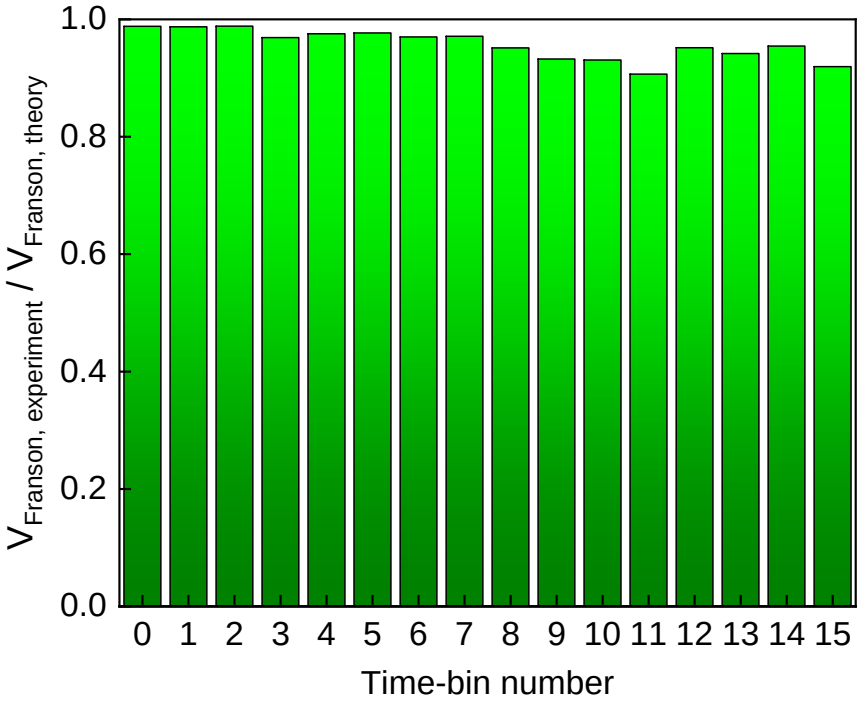

Supplementary Figure 6 | Comparison between experimental visibilities of Franson-interference recurrences for time bins 0 through 15 after 10 km asymmetric distribution of our 45.32 GHz singly-filtered BFC with theory that assumes perfect distribution.

Supplementary Note 4. Binned Schmidt-mode decompositions of the singly-filtered biphoton frequency comb in the time- and frequency-domains

In this section we report the Schmidt eigenvalues and Schmidt numbers for the frequency-binned and time-binned 45.32 GHz singly-filtered BFC. Supplementary Table 1 presents the frequency-binned Schmidt eigenvalues extracted from the frequency-bin correlation measurements in the main text's Figure 1c. These eigenvalues were obtained from performing a Schmidt decomposition of the frequency-correlation matrix [S6-S9] under the assumption that the BFC's joint spectral amplitude equals the square-root of its joint spectral intensity.

Supplementary Table 1 | Measured frequency-bin Schmidt eigenvalues and Schmidt number for the 45.32 GHz singly-filtered BFC.

Frequency-bin number	Schmidt eigenvalues	Schmidt number
2	0.119	4.17
1	0.228	
0	0.355	
-1	0.191	
-2	0.106	

As explained in the main text's Methods section, the Schmidt mode decomposition for the time-binned 45.32 GHz singly-filtered BFC is derived from the visibilities of the Franson-interference recurrences. Evaluating the main text's approximate (unnormalized) time-domain biphoton wave function at the Franson-interference recurrence times we get,

$$\Psi(n\Delta T) = \exp(-n\Delta\omega\Delta T)\sum_{m=-N}^{n}\operatorname{sinc}(Am\Delta\Omega), \tag{10}$$

from which it readily follows that the nth bin's visibility is $V_n = \exp(-n\Delta\omega\Delta T)$, as stated in the main text. Equation (10) then leads to the main text's theoretical expressions for the time-binned Schmidt eigenvalues $\{\lambda_n\}$, and its Schmidt number K_T:

$$\lambda_n = \frac{\mathrm{e}^{-\pi n/F}}{\sum_{m=0}^{M}\mathrm{e}^{-\pi m/F}}, \text{ for } 0 \le n \le M, \tag{11}$$

and

$$K_T = \frac{\sinh^2[\pi(M+1)/2F]\sinh(\pi/F)}{\sinh^2(\pi/2F)\sinh[\pi(M+1)/F]}, \tag{12}$$

where M+1 is the number of time bins and F is the FFPC's finesse. Assuming, as discussed in the main text, that the time-binned singly-filtered BFC's joint temporal amplitude equals the square root of its joint temporal intensity, the experimental time-binned Schmidt eigenvalues and Schmidt number are

$$\lambda_n = \frac{V_n}{\sum_{m=0}^{M}V_n}, \text{ for } 0 \le n \le M, \tag{13}$$

and

$$K_T = \frac{(\sum_{n=0}^{M}V_n)^2}{\sum_{n=0}^{M}V_n^2}. \tag{14}$$

We do not, however, expect the approximate time-binned biphoton wave function to be as accurate for the singly-filtered BFC as it is for the doubly-filtered BFC, because the slower frequency-domain fall off with only the signal being FFPC filtered leads to greater overlap between the contributions from adjacent and near-adjacent cavity resonances that are not properly accounted for in Eq. (1). So, to test the validity of using the *experimental* visibilities in Eqs. (13) and (14) to obtain the time-binned singly-filtered BFC's Schmidt eigenvalues and Schmidt number we compared two *theoretical* approaches to obtaining those Schmidt eigenvalues. The first approach used the exact frequency-domain biphoton wave function from Eq. (2) to calculate the Franson visibilities, as described in Supplementary Note 3.A, and used those visibilities in Eq. (13) to obtain the time-binned Schmidt eigenvalues. The second approach took the numerical inverse Fourier transform of Eq. (2) to obtain the (unnormalized) time-domain biphoton wave function, $\Psi(n\Delta T)$, at the recurrence times, and used that in Eq. (13) in place of the V_n to get the Schmidt eigenvalues. Both calculations used the source parameters for our 45.32 GHz single-resonant BFC. The results of these calculations – which are compared in Supplementary Figure 7 – are nearly identical, with a maximum normalized error of 0.38% for any of the 16 time bins.

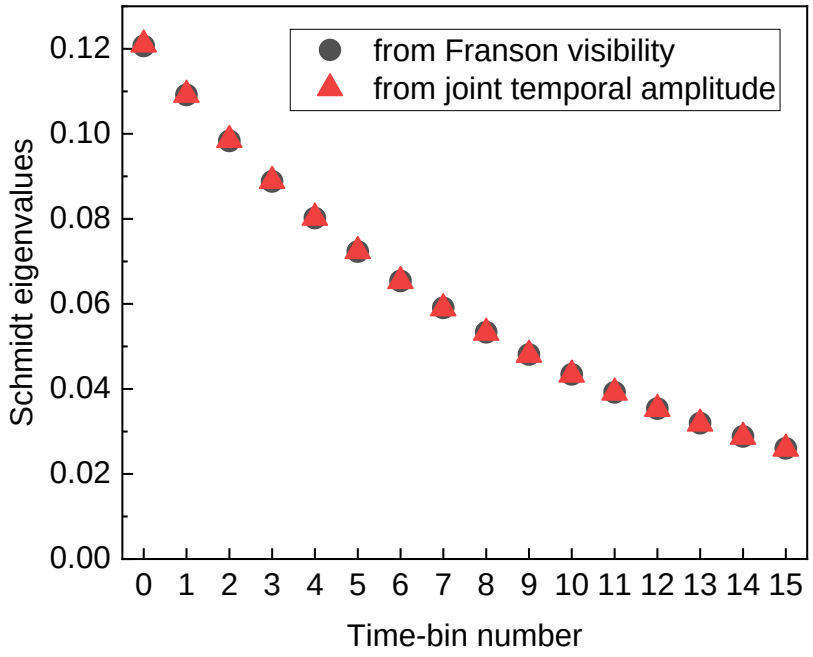

Supplementary Figure 7 | Theoretical time-binned Schmidt eigenvalues for the 45.32 GHz singly-filtered BFC calculated by: (1) using the Franson-interference visibilities, obtained as described in Supplementary Note 3.A, in Eq. (13) to get the Schmidt eigenvalues (blue open circles); and (2) using the (unnormalized) joint temporal amplitude, found by numerical inverse

Fourier transformation of Eq. (3), in place of V_n in Eq. (13) to get the Schmidt eigenvalues (orange open triangles). The two approaches yield eigenvalues that are nearly identical, with a maximum of 0.38% normalized error for any of the 16 bins.

Supplementary Table 2 shows the measured time-bin Schmidt eigenvalues and Schmidt number for the 45.32 GHz singly-filtered BFC before and after the 10 km entanglement distribution. Its 13.11 Schmidt number is in excellent agreement with the 13.19 theoretical value obtained using the exact theory based on Eq. (2). After the 10 km distribution, we obtained the Schmidt number of 12.99, showing only a 0.92% degradation.

Supplementary Table 2 | Measured time-bin Schmidt eigenvalues and Schmidt number for the 45.32 GHz singly-filtered BFC before and after 10 km distribution.

Time-bin number	Singly-resonant BFC			After 10 km distribution		
	Franson Visibilities	Schmidt eigenvalues	Schmidt number	Franson Visibilities	Schmidt eigenvalues	Schmidt number
0	0.9946	0.122	13.11	0.9881	0.123	12.99
1	0.9017	0.110		0.8928	0.111	
2	0.8103	0.099		0.8054	0.101	
3	0.7282	0.089		0.7128	0.089	
4	0.656	0.080		0.6481	0.081	
5	0.5957	0.073		0.5854	0.073	
6	0.5403	0.066		0.5257	0.066	
7	0.4868	0.059		0.4752	0.059	
8	0.4354	0.053		0.4203	0.052	
9	0.3879	0.047		0.3718	0.046	
10	0.3371	0.041		0.335	0.042	
11	0.3147	0.038		0.2946	0.037	
12	0.2912	0.036		0.279	0.035	
13	0.2593	0.032		0.2493	0.031	
14	0.2379	0.029		0.2279	0.028	
15	0.2058	0.025		0.1983	0.025	

Supplementary Note 5. Low-jitter SNSPDs for temporal correlation measurements

Impedance-matched differential SNSPDs have recently been developed in order to simultaneously achieve a practical active area for efficient coupling to a single mode fiber and low-jitter operation [S10]. The two detectors used in this work had optical stacks based on a double anti-reflection coating above the nanowire, optimized for 1550 nm, resulting in an efficiency of ≈ 80% at this wavelength with ≈ 13.1 ps. In the O-band, the efficiency is expected to be on the order of the 10%. By redesigning the optical stack, it would be possible to achieve 80% efficiency at 1310 nm in the future. The impedance-matching in SNSPDs significantly improves the signal-to-noise ratio of the readout, thus even though cryogenic amplifiers were not used in this work, the system timing jitter, including the time tagger (Swabian Time Tagger X) was on the order of 15 ps. To characterize the effective timing-jitter of the experiment, we measured the cross-correlation between signal and idler photons of our O-Band SPDC source in Supplementary Figure 8 and obtained 21.6 ps. This matches the expected summation in quadrature of the two detectors with 15 ps jitter. Excluding the electronic jitter from the time tagger system (≈ 4.7 ps, Time Tagger X), we estimate the intrinsic timing jitter of the SNSPDs to be ≈ 14.5 ps in the O band. We expect that in the future it will be possible to improve the detector jitter further through the use of faster superconducing materials and improvements in nanofabrication [S4] which would resolve the temporal correlation of BFCs with even higher cavity free-spectral range.

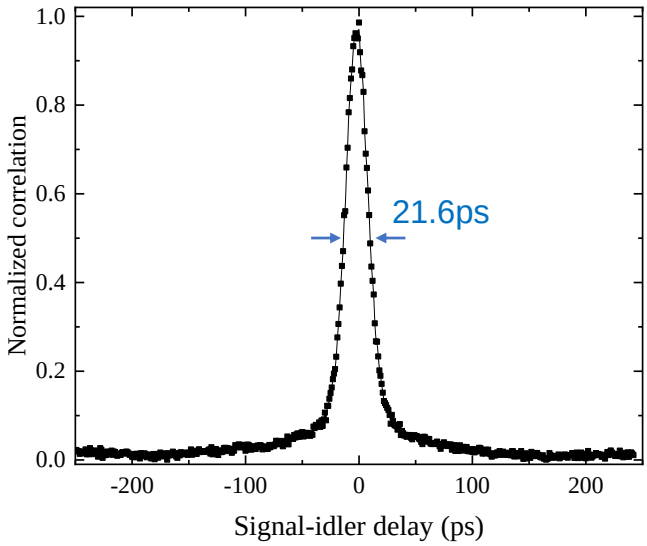

Supplementary Figure 8. Effective timing jitter characterization of the two low-jitter SNSPDs. The full-width-half-maximum of the cross-correlation is measured to be 21.6 ps using our SPDC source in the O band. The intrinsic timing jitter of the SNSPDs is estimated to be ≈ 14.5 ps.

Supplementary Note 6. Franson-interference recurrences for frequency-bin pairs

Here, in Supplementary Figure 9, we present the measured Franson-interference patterns for all 25 frequency-bin pairs within our source's bandwidth. The visibilities extracted from these interference patterns were shown as the visibility map in main text's Figure 3b. Due to SPDC's energy conservation, only frequency-correlated photon pairs show energy-time entanglement in our singly-filtered BFC. Therefore, only the symmetric frequency-bin pairs exhibit high Franson interference visibilities in Supplementary Figure 9, with average raw visibility of 87.25%. As the frequency-bin pairs move away from frequency degeneracy, both their singles and coincidence rates decrease because of the SPDC phase-matching function. The reduced number of coincidences ultimately become comparable to the accidentals. Indeed, measurements on uncorrelated frequency-bin pairs, show no obvious fringes and their coincidence counts are almost at the noise floor. Thus, in Supplementary Figure 9 we did *not* subtract accidental coincidences, but we did do that subtraction in the main text's Figure 3a because there we only showed the 5 symmetric frequency-bin pairs. Also, after 10 km asymmetric entanglement distribution, we chose to make Franson interference measurements only for the symmetric frequency-bin pairs, see the interference fringes shown in the main text's Figure 4a inset.

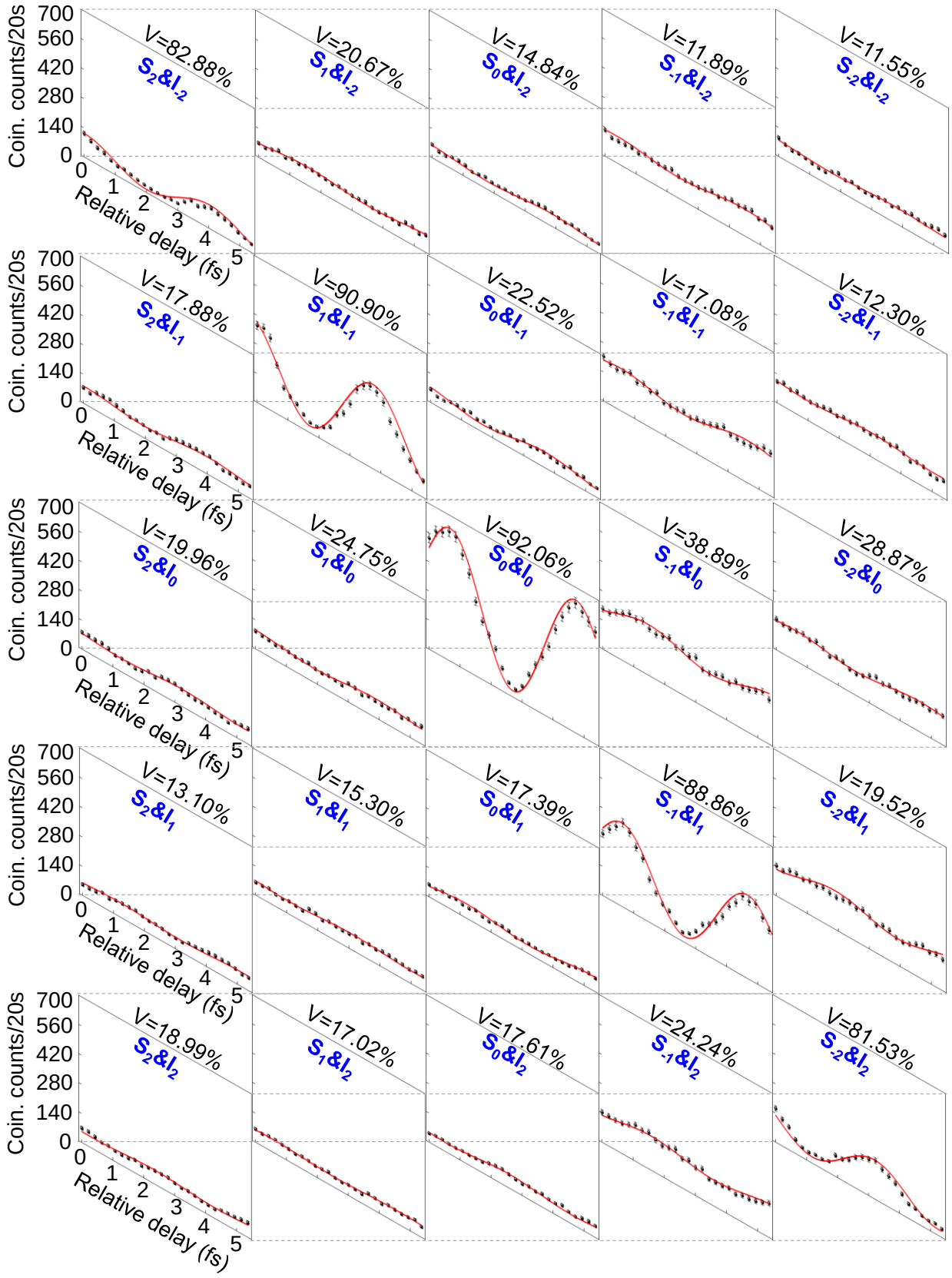
Coin. counts/20s
700
560
420
280
140
0
0 1 2 3 4 5
Relative delay (fs)
V=82.88%
S2&I-2
V=20.67%
S1&I-2
V=14.84%
S0&I-2
V=11.89%
S-1&I-2
V=11.55%
S-2&I-2
V=17.88%
S2&I-1
V=90.90%
S1&I-1
V=22.52%
S0&I-1
V=17.08%
S-1&I-1
V=12.30%
S-2&I-1
V=19.96%
S2&I0
V=24.75%
S1&I0
V=92.06%
S0&I0
V=38.89%
S-1&I0
V=28.87%
S-2&I0
V=13.10%
S2&I1
V=15.30%
S1&I1
V=17.39%
S0&I1
V=88.86%
S-1&I1
V=19.52%
S-2&I1
V=18.99%
S2&I2
V=17.02%
S1&I2
V=17.61%
S0&I2
V=24.24%
S-1&I2
V=81.53%
S-2&I2

Supplementary Figure 9 | Franson interference fringes for 25 frequency-bin pairs of the 45.32 GHz singly-filtered BFC. Frequency-bin pairs and corresponding visibilities are denoted for each interference pattern, with high interference visibilities only occurring for symmetric frequency-bin pairs. The error bars represent one standard deviation of the mean assuming Poissonian statistics.

Supplementary Note 7. Photon information efficiency and secret key rate of frequency-multiplexed quantum key distribution using the singly-filtered biphoton frequency comb

Quantum key distribution with the singly-filtered BFC was demonstrated using high-dimensional time-bin encoding protocol. The proof-of-principle QKD experiment was performed without 10 km distribution fiber due to the limited electronic delay compensation of our time tagging electronics (PicoHarp 300). Alice had the SPDC source and retained the FFPC-filtered signal photons while sending the unfiltered idler photons to Bob via single-mode fiber. Correlated frequency bins were selected at Alice and Bob's terminals using demultiplexing filters. Part of their filtered light was then directed to SNSPDs for raw-key generation while the rest was sent to their halves of the Franson interferometer for the security check. For key generation, Alice and Bob recorded a 10-second-long time stream of photon detections for post-detection processing. During this post-processing, their time streams were synchronized and divided into time-bins for discretization with variable bin durations. The bins were grouped into frames of 2^N bins, where N is the number of encoded bits per photon. For each frame we compared Alice and Bob's raw timestamps and discarded frames in which Alice and Bob did not each record a single count. This procedure resulted in a raw keystream comprised of the binary numbers that Alice and Bob assigned to their respective symbols – i.e., the bin number of their respective counts – in each frame. The raw keystream has two types of symbol errors, viz., global errors, which are due to a combination of photon losses and dark counts, and local errors, which are due to the detectors' timing jitter. Global errors result in large discrepancies between Alice and Bob's raw-keystream bin numbers, whereas local errors result small bin-number errors. To achieve information reconciliation in the presence of these error types we use the layered low-density parity-check code from Refs. [S11, S12]. Using this code, we have calculated the Shannon information upper bound on the photon information efficiency (PIE), the bits we can send per photon under highly-erroneous channel conditions. We have collected keystreams and encoded them using different discretization bin widths and encoded number of bits. After calculating PIEs for each, we have multiplied each PIE with the number of photon pairs per second in the corresponding keystream to obtain the key

rate. So far, we have encoded PIE up to ≈ 14 bits/photon using our frequency multiplexed SR BFC (in main text Figure 4d), and the total key rate of ≈ 4.7 kbits/s. We expect the key rate can be improved either by using a higher brightness entangled photon source [S13], or by utilizing a cavity-enhanced SPDC configuration to generate a singly-filtered BFC [S14].

The photon information efficiency and key rate is maximized by finding optimal bin width and frame sizes, as shown in Supplementary Figure 10a and 10b. Smallest bin width and highest number of encoded bits, i.e., the largest frame size, are desired for maximum key rate. However, the bin width is limited by the timing uncertainty between signal and idler, which is 210.2 ps for this experiment. This leads to a lower performance when bin width is decreased to 100 ps as shown in Supplementary Figure 11. Similarly, maximum frame size is limited by the biphoton coherence time, however a more realistic bound is the detector dead time. If the frame size is too large, it causes symbol errors, due to accidental coincidences, that are uniformly distributed over the frame. Because of this fact, the increase in PIE and key rate reduces after 6 bits encoding for the central bin pair, as shown in Supplementary Figure 10a and 10b. This reduction starts at a smaller frame size of 2^5 for frequency-bin pairs S_2&I_{-2} and S_{-2}&I_2. PIE peaks at 7 bits encoding then decreases due to interaction of more accidental coincident frames used for erroneous symbol generation. The ratio of correct symbols versus all the generated frames is given in Supplementary Figure 11c. It reflects the fact that error increases with (a) bin width closer or lower than coincidence uncertainty and (b) frame sizes larger or close to detector dead time, leading to more accidental frame pairs possessing symbol errors.

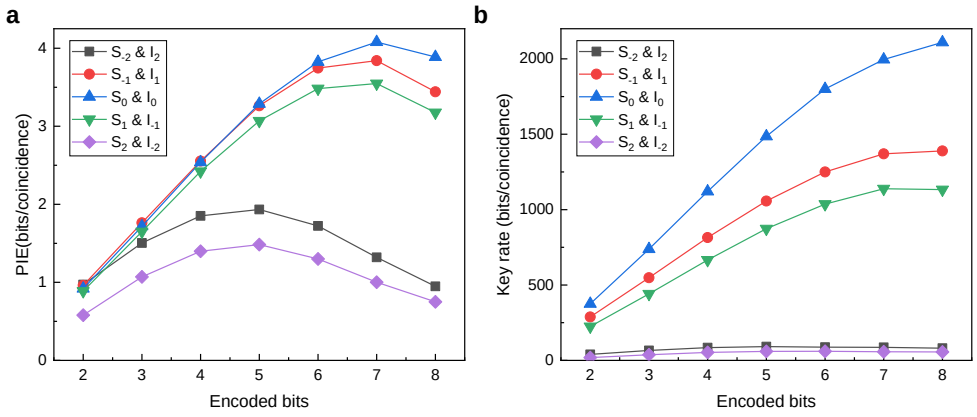

Supplementary Figure 10 | a, Photon information efficiency in number of effective transmitted bits per coincidence for each entangled conjugate frequency-bin pair. The maximum number of transmitted bits per coincidence is ~ 4.1 bits/coincidence, transmitted over the S_0&I_0 frequency-

bin pair. **b,** The key rates are obtained using the BFC generation rate when the ppKTP waveguide is pumped at 2.3 mW. The total key rate propagated over five channels is up to 4.7 kbits/s.

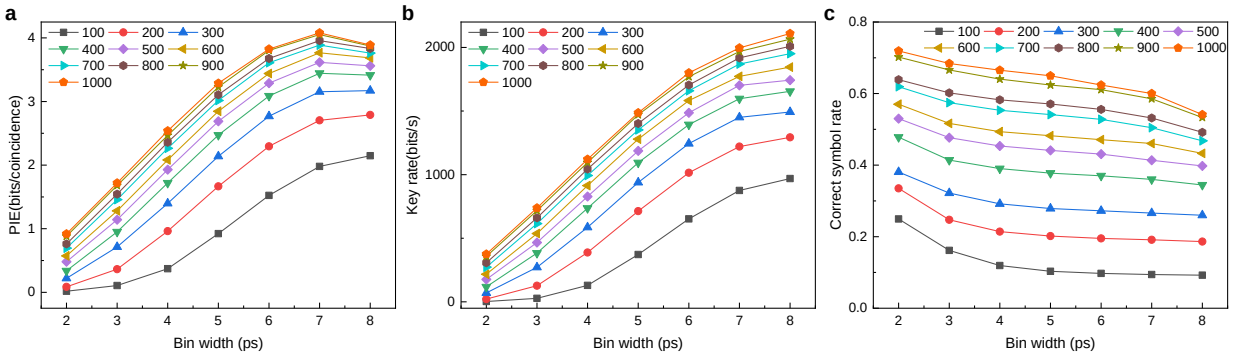

Supplementary Figure 11 | a, Changes in the S_0&I_0 channel's PIE with frame size as determined by the bin width (discretization duration) and number of encoded bits. **b,** Changes in the S_0&I_0 channel's key rate with frame size as determined by the bin width (discretization duration) and number of encoded bits. **c,** The ratio of correctly propagated symbols versus all the transmitted frames, for channel S_0&I_0 as an example.

To check the security of the frequency-multiplexed channel, the measured degradation of the Franson-interference visibility V from its theoretical value V_{th} was used as a signature of eavesdropping to terminate the communication if the degradation was too strong. Otherwise, V_{th}-V was used to determine the frequency anti-correlation between signal and idler by [S15]:

$$\Delta\langle\Delta\widehat{\omega_S}^2 - 2\Delta\widehat{\omega_S}\Delta\widehat{\omega_I}\rangle \leq 2(V_{th} - V)/\Delta T_F^2, \quad (17)$$

where ΔT_F is the relative delay between arm 1 and arm 2 of the Franson interferometer, $\Delta\widehat{\omega_S}$ ($\Delta\widehat{\omega_I}$) is the frequency operator measuring the zero-mean frequency detuning from degeneracy of the signal (idler) photon. The frequency anti-correlation information was then used to construct a time-frequency covariance matrix to compute an upper bound on Eve's Holevo information from which the secret-key rate can be found for the chosen frequency-bin pair [S15, S16]. This upper bound represents the worst case of Eve's Holevo information and is then used to calculate the most pessimistic secure PIE. Supplementary Table 3 summarizes the calculated Eve's Holevo information upper bound for each frequency-bin pair. Comparing with the highest PIE shown in Supplementary Figure 10, we obtain secure key rate over three correlated frequency-bin pairs with positive secure PIE. A total secure key rate of ~1.1 kbits/s is achieved over S_1&I_{-1}, S_0&I_0 and S_{-1}&I_1, as shown in main text's Figure 4e.

Supplementary Table 3 | Eve's Holevo information upper-bounded by measured Franson visibility for each frequency-bin pair.

Frequency-bin pair	Franson visibility	Eve's Holeve information upper bound	Secured PIE
S_2&I_{-2}	0.9724	3.811	0
S_1&I_{-1}	0.9842	3.402	0.424
S_0&I_0	0.9966	2.233	1.846
S_{-1}&I_1	0.9838	3.421	0.146
S_{-2}&I_2	0.9645	3.995	0

Supplementary References

[S1] F. N. C. Wong, J. H. Shapiro, and T. Kim, Efficient generation of polarization-entangled photons in a nonlinear crystal, *Laser Phys.* **16**, 1517 (2006).

[S2] J. H. Shapiro, Dispersion cancellation with phase-sensitive Gaussian-state light, *Phys. Rev. A* **81**, 023824 (2010).

[S3] U. Herzog, M. Scholz, and O. Benson, Theory of biphoton generation in a single-resonant optical parametric oscillator far below threshold, *Phys. Rev. A* **77**, 023826 (2008).

[S4] B. Korzh, Q.-Y. Zhao, J. P. Allmaras, S. Frasca, T. M. Autry, E. A. Bersin, A. D. Beyer, R. M. Briggs, B. Bumble, M. Colangelo, G. M. Crouch, A. E. Dane, T. Gerrits, A. E. Lita, F. Marsili, G. Moody, C. Peña, E. Ramirez, J. D. Rezac, N. Sinclair, M. J. Stevens, A. E. Velasco, V. B. Verma, E. E. Wollman, S. Xie, D. Zhu, P. D. Hale, M. Spiropulu, K. L. Silverman, R. P. Mirin, S. W. Nam, A. G. Kozorezov, M. D. Shaw, and K. K. Berggren, Demonstration of sub-3 ps temporal resolution with a superconducting nanowire single-photon detector, *Nat. Photon.* **14**, 250 (2020).

[S5] J. Zhao, C. Ma, M. Rüsing, and S. Mookherjea, High quality entangled photon pair generation in periodically poled thin-film lithium niobate waveguides, *Phys. Rev. Lett.* **124**, 163603 (2020).

[S6] J. H. Eberly, Schmidt analysis of pure-state entanglement, *Laser Phys.* **16**, 921 (2006).

[S7] J. Mosley, J. S. Lundeen, B. J. Smith, and I. A. Walmsley, Conditional preparation of single photons using parametric downconversion: a recipe for purity, *New J. Phys.* **10**, 093011 (2008).

[S8] J. A. Jaramillo-Villegas, P. Imany, O. D. Odele, D. E. Leaird, Z.-Y. Ou, M. Qi, and A. M. Weiner, Persistent energy–time entanglement covering multiple resonances of an on-chip biphoton frequency comb, *Optica* **4**, 655 (2017).

[S9] K. Zielnicki, K. Garay-Palmett, D. Cruz-Delgado, H. Cruz-Ramirez, M. F. O'Boyle, B. Fang, V. O. Lorenz, A. B. U'Ren, and P. G. Kwiat, Joint spectral characterization of photon-pair sources, *J. Mod. Optics* **65**, 1141 (2018).

[S10] M. Colangelo, B. Korzh, J. P. Allmaras, A. D. Beyer, A. S. Mueller, R. M. Briggs, B. Bumble, M. Runyan, M. J. Stevens, A. N. McCaughan, D. Zhu, S. Smith, W. Becker, L. Narváez, J. C. Bienfang, S. Frasca, A. E. Velasco, C. H. Peña, E. E. Ramirez, A. B. Walter, E. Schmidt, E. E. Wollman, M. Spiropulu, R. Mirin, S. W. Nam, K. K. Berggren, M. D. Shaw, Impedance-matched differential superconducting nanowire detectors, *arXiv:2108.07962* (2021).

[S11] H. Zhou, V. Chandar, and G. Wornell, Low-density random matrices for secret key extraction, *In 2013 IEEE International Symposium on Information Theory* (pp. 2607-2611), IEEE.

[S12] H. Zhou, L. Wang, and G. Wornell, Layered schemes for large-alphabet secret key distribution, *In 2013 Information Theory and Applications Workshop (ITA)* (pp. 1-10), IEEE.

[S13] G.-T. Xue, Y.-F. Niu, X. Liu, J.-C. Duan, W. Chen, Y. Pan, K. Jia, X. Wang, H.-Y. Liu, Y. Zhang, P. Xu, G. Zhao, X. Cai, Y.-X. Gong, X. Hu, Z. Xie, and S. Zhu, Ultra-bright multiplexed energy-time entangled photon generation from lithium niobate on insulator chip, *Phys. Rev. Appl.* **15**, 064059 (2021).

[S14] R. Ikuta, R. Tani, M. Ishizaki, S. Miki, M. Yabuno, H. Terai, N. Imoto, and T. Yamamoto, Frequency-multiplexed photon pairs over 1000 modes from a quadratic nonlinear optical waveguide resonator with a singly resonant configuration, *Phys. Rev. Lett.* **123**, 193603 (2019).

[S15] T. Zhong, H. Zhou, R. D. Horansky, C. Lee, V. B. Verma, A. E. Lita, A. Restelli, J. C. Bienfang, R. P. Mirin, T. Gerrits, S. W. Nam, F. Marsili, M. D. Shaw, Z. Zhang, L. Wang, D. Englund, G. W. Wornell, J. H. Shapiro, and F. N. C. Wong, Photon-efficient quantum key distribution using time–energy entanglement with high-dimensional encoding, *New J. Phys.* **17**, 022002 (2015).

[S16] Z. Zhang, J. Mower, D. Englund, F. N. C. Wong, and J. H. Shapiro, Unconditional security of time-energy entanglement quantum key distribution using dual-basis interferometry, *Phys. Rev. Lett.* **112**, 120506 (2014).